Available online at www.sciencedirect.com
ScienceDirect
International Journal of Heat and Mass Transfer 51 (2008) 312–326
International Journal of HEAT and MASS TRANSFER
www.elsevier.com/locate/ijhmt

A multifunctional heat pipe sandwich panel structure

Douglas T. Queheillalt [a,*], Gerardo Carbajal [b], G.P. Peterson [c], Haydn N.G. Wadley [a]

[a] University of Virginia, Department of Materials Science and Engineering, 140 Chemistry Way, P.O. Box 400745, Charlottesville, VA 22904, USA
[b] University of Turabo, School of Engineering, P.O. Box 3030, Gurabo 00778, Puerto Rico
[c] University of Colorado at Boulder, 914 Broadway, Boulder, CO 80309, USA

Received 27 August 2006; received in revised form 30 March 2007
Available online 18 June 2007

Abstract

A multifunctional sandwich panel combining efficient structural load support and thermal management characteristics has been designed and experimentally assessed. The concept is based upon a truncated, square honeycomb sandwich structure. In closed cell honeycomb structures, the transport of heat from one face to the other occurs by a combination of conduction through the webs and convection/radiation within the cells. Here, much more effective heat transport is achieved by multifunctionally utilizing the core as a heat pipe sandwich panel. Its interior consists of a 6061 aluminum truncated-square honeycomb core covered with a stochastic open-cell nickel foam wick. An electroless nickel plating barrier layer inhibited the chemical reaction between the deionized water working fluid and the aluminum structure, retarding the generation of non-condensable hydrogen gas. A thermodynamic model was used to guide the design of the heat pipe sandwich panel. We describe the results of a series of experiments that validate the operational principle of the multifunctional heat pipe sandwich panel and characterize its transient response to an intense localized heat source. The systems measured thermal response to a localized heat source agrees well with that predicted by a finite difference method model used to predict the thermal response.

Keywords: Cellular material; Heat pipe; Honeycomb; Multifunctional structures

1. Introduction

Recent research indicates that lattice truss sandwich structures can be highly efficient load supporting systems when configured as the cores of sandwich panels. This arises when the core ligaments are oriented such that during panel bending they are subjected to compressive or stretching loads rather than the bending moments [1]. These cellular metal lattice structures [2] and simple methods for making [3,4] them are gaining interest for use as multifunctional structures which offer efficient structural load support and additional functionalities such as mechanical (impact) energy absorption [5,6], various forms of thermal management [7,8] and numerous shape morphing possibilities [9–11].

Lattice structures possess very low flow resistance pathways within their core region [12–14]. When fabricated from high thermal conductivity materials, sandwich panels with lattice cores have been shown to be efficient cross flow heat exchangers [7,8]. Assume, a localized heat flux is applied to one facesheet of a sandwich panel. The thermal energy absorbed can be spatially dispersed within the core via conduction and then dissipated to a cross flowing fluid that passes through the core with little frictional resistance [7,8]. Initial research indicates that these structures are promising candidates for very lightweight, multifunctional structures which combines efficient load support and one form of thermal management.

As structural loads rise, the core relative density must also be increased to avoid plastic deformation [2]. As the core relative density increases above ~2–4%, honeycomb structures become slightly more structurally efficient than their lattice counterparts [4]. However, honeycomb

* Corresponding author. Tel.: +1 434 982 5678; fax: +1 434 982 5677.
E-mail address: dougq@virginia.edu (D.T. Queheillalt).

0017-9310/$ - see front matter © 2007 Elsevier Ltd. All rights reserved.
doi:10.1016/j.ijheatmasstransfer.2007.03.051

Nomenclature

C	specific heat, J/(kg K)
d	foam pore diameter, mm
ΔT	temperature difference, K
g	gravitational constant, m/s^2
h	height of liquid within capillary tube, cm
l	center-to-center cell spacing, mm
m	mass, kg
N	figure of merit, kW/m^2
P	pressure, Pa
Q	net heat capacity, J
r	capillary tube radius, mm
t	web thickness, mm
T	temperature, K
U	specific internal energy, J/kg
v	specific volume, m^3/kg
V	volume, m^3
w	web length, mm
x	quality

Greek symbols

α	deviation factor
δ	wick thickness, mm
θ	angle between the liquid–vapor interface and solid surface
ρ	density, kg/m^3
$\bar{\rho}$	relative density
σ	surface tension, N/m
σ_{pk}	peak compression strength, MPa
σ_y	yield strength, MPa
Σ	lattice topology factor

Subscripts

0	initial (reference) state
Al	aluminum
f	final (reference) state
i	initial (reference) state
l	liquid
Ni	nickel
w	water
v	vapor

structures are closed celled which precludes them from being used as cross flow heat exchanges [15–18]. The dissipation of a localized thermal flux applied to one surface of a honeycomb sandwich structure occurs by conductive transport over the heated facesheet and within the core elements to the opposite facesheet. Convective and radiative mechanisms within and across the cells can also occur. The applied heat flux can eventually be rejected to the ambient air via natural or forced convection and radiative processes over the opposite facesheet. The rate of thermal transport within such a panel depends on the thermal conductivity of the facesheets/webs, the core volume fraction and the effectiveness of the convective and radiative transport mechanisms within the core cells. On one hand, when very low relative density cores made from high thermal resistivity materials are used, the conductive heat transfer process is impeded, and these structures then provide excellent through thickness thermal insulation characteristics. On the other hand, good thermal spreading (and dissipation) to surroundings can be achieved using higher relative density cores made from high thermal conductivity metals, especially if high internal gas pressures can be used to enhance convective transport within the core. However, the effectiveness of the convective mechanism will be limited by low thermal conductivities of most gases and its confinement within a honeycomb cell. Much more effective transport could be achieved if the convective processes within the sandwich structure could be better exploited. It is argued here, that heat pipe/plate structures provide a potentially effective means for doing this [19].

Heat pipes are hollow structures that contain large diameter voids connecting regions close to a source of heat with others that are cooler. The interior surfaces of these hollow spaces are covered with a fluid saturated wick that facilitates capillary driven fluid flow. Once evacuated and sealed, the system acts like a closed-loop, two-phase convective thermal transport system [19]. Heat applied locally to the structure evaporates the fluid and the vapor is then rapidly transported to cooler regions where condensation occurs. The evaporating liquid in the hot (evaporator) part of the system is continually replenished by capillary pumping of fluid that has condensed in the cooler region of the structure. The evaporation results in a local pressure increase and creates a pressure gradient that can enhance vapor flow from the hot evaporator region to a cooler condenser region. The vapor in some heat pipe designs can travel rapidly to the condenser, where it condenses, releasing the latent of heat condensation. This can serve as a very rapid means for transporting thermal energy and isothermalizing locally heated structures acting as though they have a very high "effective" thermal conductivity. A flat heat pipe is therefore potentially able to produce a large surface area with a very small temperature gradient. Heat pipe/plate structures can also possess very high specific thermal capacities (because of the usually high latent heat of vaporization of the working fluids).

Several honeycomb sandwich panel plate concepts have been evaluated for use as heat plate radiators on space platforms [20–22]. Fabricated from stainless steel, these structures utilize hexagonal honeycomb cells with circular

holes cut in the webs to allow lateral vapor flow between cells. Either ammonia or methanol are compatible working fluids for stainless steel systems and possess high surface tensions and latent heats in the −20 to 65 °C temperature range [19]. Thermophotovoltaic energy conversion systems utilizing flat heat pipes have also been proposed [23,24]. These systems were constructed from Monel 400 which facilitates the use of water as the working fluid for operations below ~100 °C. Much higher temperatures can be achieved by the use of liquid metal working fluids. For example stainless steel structures utilizing hexagonal honeycomb cells (again with perforated webs) and either cesium, potassium or sodium as the working fluid have been used for operation at temperatures of ~650 °C [25–27].

For capillary wick limited heat pipes, a liquid transport factor or figure of merit, N, which governs the characteristics of a good heat pipe working fluid: high latent heat of vaporization, high surface tension, high liquid density, and low liquid viscosity. The figure of merit can be used to describe the effectiveness of working fluid at a specific operating temperature. In the temperature range of interest here, water possesses the highest value of N. In addition, water is the preferred working fluid for many applications because it is odorless, nontoxic and nonflammable. Multifunctional thermal spreading devices based upon high specific strength aluminum alloys that utilize water as the working fluid would be highly desirable for many aerospace applications. However, the use of water in conjunction with aluminum results in the rapid generation of hydrogen gas which collects as a thermally insulating gas in the condenser region [28]. This degrades the performance of the heat pipe, and if large amounts of hydrogen are generated, can lead to safety issues [29]. Less reactive, much higher density metals such as copper, 347 stainless steel, Monel 400 and nickel are therefore generally usually used for water filled heat pipes [30,31].

Here, we explore the use of a non-reactive nickel barrier layer applied uniformly to the interior of an aluminum honeycomb sandwich structure to enable the fabrication of a non-hydrogen generating aluminum–water heat pipe sandwich panel. We describe the design and fabrication of a truncated, square honeycomb sandwich panel made from an aluminum alloy in which all internal surfaces were coated with an electroless nickel layer and the use of a stochastic open-cell nickel foam wick system with deionized water as the working fluid. We show that the resulting multifunctional panels provide rapid thermal spreading between 25 and 150 °C. The measured temperature distributions on these panels were well predicted by finite difference analysis of the coupled heat and vapor transport within the core [32].

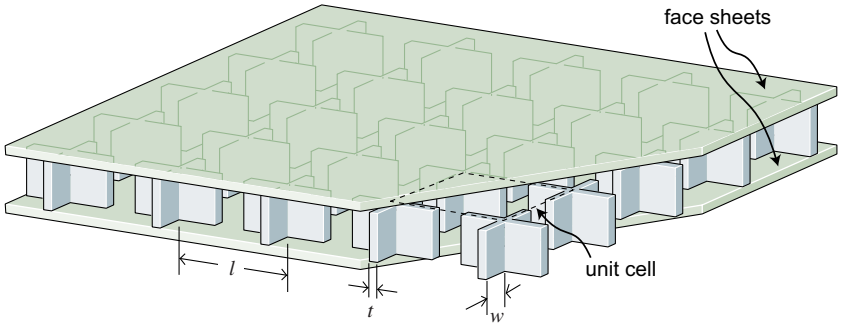

Fig. 1. A schematic illustration of the unit cell topology of a truncated-square honeycomb core used in a sandwich panel.

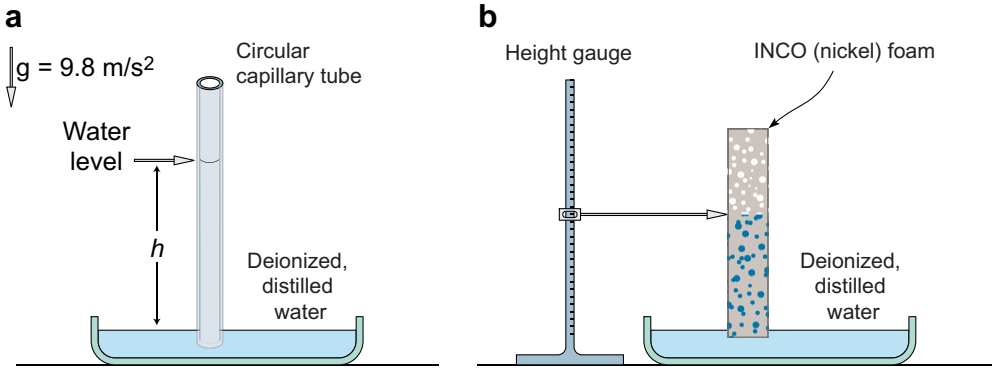

Fig. 2. Schematic illustrations of (a) a single capillary tube with one end inserted in a liquid bath and (b) compressed nickel foam strips for measurement of wicking heights.

2. Design and fabrication

2.1. Honeycomb panel design

Metal honeycomb sandwich structures with square cells are highly efficient load supporting structures [15–18]. However, these closed cell sandwich structures need to be modified to allow vapor flow within the core region if they are to be used for flat heat pipe sandwich panel applications. This can be accomplished several ways. One approach practiced in the past is to perforate each of the honeycomb walls (webs) creating circular holes [25–27]. While this allows relatively unimpeded vapor flow within the core, the holes result in stress concentrations in the webs that can significantly reduce the mechanical strength of the honeycomb structure [33–37]. An alternative, truncated-square honeycomb core topology has been employed here. By removing a region at the middle of the cell wall of a regular square honeycomb lattice, the resulting crucifix topology allows easy vapor and fluid transport laterally within the core.

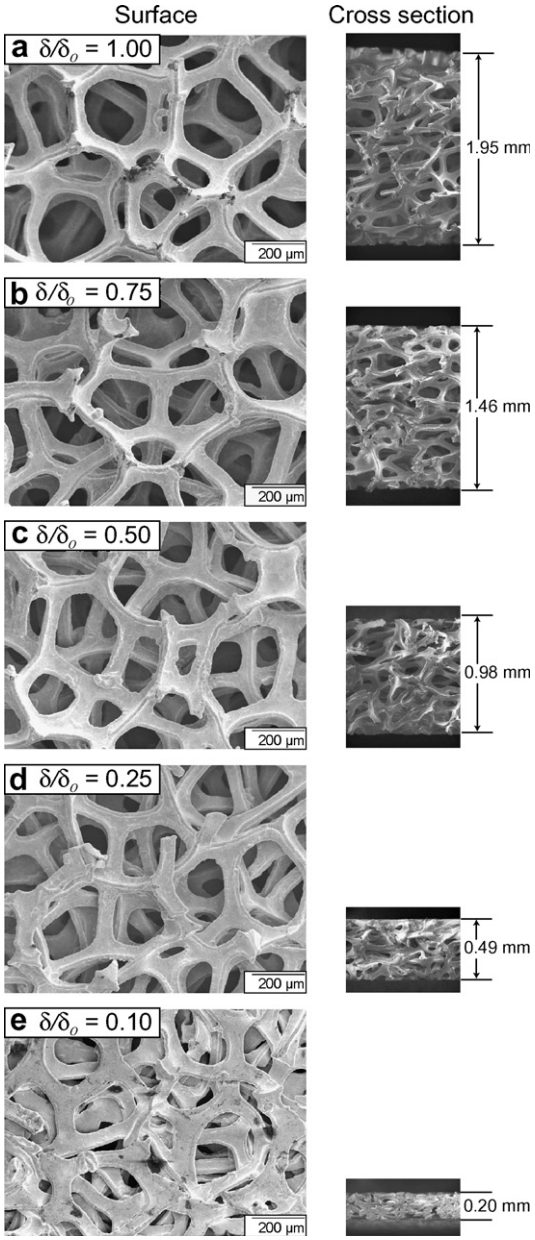

Fig. 3. Scanning electron micrographs of the surface and cross section of compressed nickel foam wicks for varying compression ratios ($\delta/\delta_0 = 1.0$, 0.75, 0.5, 0.25, 0.1).

The peak compressive strength, σ_{pk}, of honeycomb (and other lattice) structures scales linearly with the relative density; $\sigma_{pk} = \Sigma\sigma_y\bar{\rho}$ where Σ is a lattice topology dependent scaling factor and σ_y is the yield strength of the parent material (assuming core deformation occurs by plastic yielding) [2]. For honeycomb cores loaded in through thickness compression, all of the webs are aligned in the loading direction and $\Sigma = 1.0$. The structural efficiency of sandwich panels in bending can be ascertained by using analytical formulae for yielding and buckling of the core and face members that assume the core fully supports the shear forces and the faces sustain the bending moments [17]. Numerous approximations for the mechanical properties of sandwich panels with honeycomb topologies have been developed [15–18]. Recent finite element modeling of a truncated-square honeycomb structure indicates that the through thickness compressive strength and elastic modulus exhibits the same dependency upon relative density as a defect-free conventional closed cell square honeycomb [38].

The truncated-square honeycomb core topology has a cruciform shaped unit cell shown in Fig. 1. The relative density, $\bar{\rho}$, of this unit cell is given by

$$\bar{\rho} = \frac{(2l - t)\alpha}{l^2} \approx \frac{2t\alpha}{l} \quad \text{for } l \gg t \tag{1}$$

where t is the web thickness, l is the center-to-center unit cell spacing and $\alpha = 2w/l$ represents the deviation from a

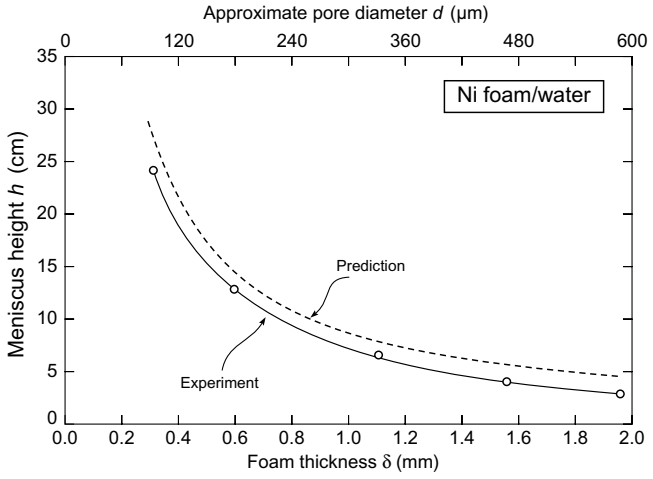

Fig. 4. Experimentally measured equilibrium pumping height for the compressed nickel foam (as well as the predicted capillary rise in a single tube of equivalent pore size) as a function of compression ratio, δ/δ_0, and the corresponding effective pore diameter, d.

regular square honeycomb (where $\alpha = 1$). For the flat heat pipe sandwich panel structure designed here, we selected, $t = 9.5$ mm, $w = 27.0$ mm, $l = 75$ mm, $\alpha = 0.71$. The relative density of the core from Eq. (1) was then 0.18.

2.2. Nickel foam wicking

During operation of a heat pipe, the evaporated working fluid is condensed and returns to the evaporator through a wick structure by liquid phase capillary pumping. As vapor is created in the evaporator a vapor pressure gradient along the vapor flow passage is created. A capillary pressure gradient in the liquid then pumps fluid from the condenser to the evaporator. The capillary pumping pressure is determined by the difference in pressure across the liquid–vapor interface which depends on the shape of the menisci that forms at the liquid–vapor interfaces [39]. This capillary pumping pressure is important since it dictates the distance a liquid can be pumped against gravity within the wick structure. For certain geometries, long pumping distances are preferred since they prevent local dry-out during heat pipe operation.

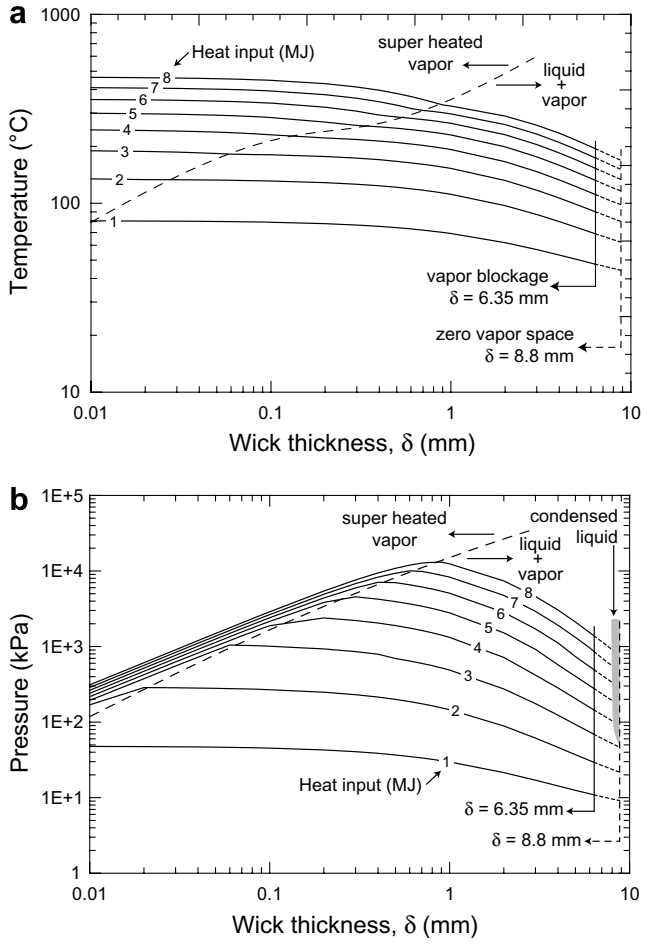

Fig. 5. (a) The temperature and (b) pressure within a flat heat pipe sandwich panel as a function of effective wick thickness for various heat inputs. Note the three distinct operational domains: super heated vapor, two-phase liquid plus vapor and condensed liquid.

An INCOFOAM® nickel foam was selected as the wicking material for the flat heat pipe system. This high-purity (>99.98 wt.%) stochastic open-cell foam is produced by chemical vapor deposition of nickel tetracarbonyl ($Ni(CO)_4$) onto an open-cell polyurethane substrate, followed by a high-temperature (~1000 °C) evaporation of the polymer template and sintering the nickel ligaments [40]. The as-received nickel foam had a thickness of 1.95 mm and an area density of 500 g/m^2 which corresponds to a relative density of 0.03. The cell size of the as-received foam was 90 pores per inch (PPI) which corresponds to an average cell diameter of ~600 μm.

If such a porous solid is approximated as an array of parallel capillary tubes, the rise in height against a gravitational force for an incompressible fluid can be estimated by balancing the hydrostatic and capillary forces using the Young–Laplace equation, Fig. 2a [41]. If P_v and P_l are the pressures in the vapor and liquid phases within a capillary tube of internal radius, r, and the capillary pressure is defined as $(P_v - P_l)$ then:

$$P_v - P_l = \frac{2\sigma\cos\theta}{r} \tag{2}$$

where σ is the surface tension of the liquid and θ is the contact angle of the liquid with the metal surface.

Assuming equilibrium between pumping and gravitational forces exists, the height of the liquid within a capillary tube oriented parallel with the gravitational force is given by

$$h = \frac{2\sigma\cos\theta}{gr(\rho_l - \rho_v)} \tag{3}$$

where g is the acceleration due to gravity (9.8 m/s^2) and ρ_v and ρ_l are the densities of the vapor and liquid phases [42]. Assuming, $\sigma = 0.061$ N/m, $\rho_l = 958.3$ kg/m^3, $\rho_v = 0.597$ kg/m^3 and ideal wetability ($\cos\theta = 1$) for liquid water in

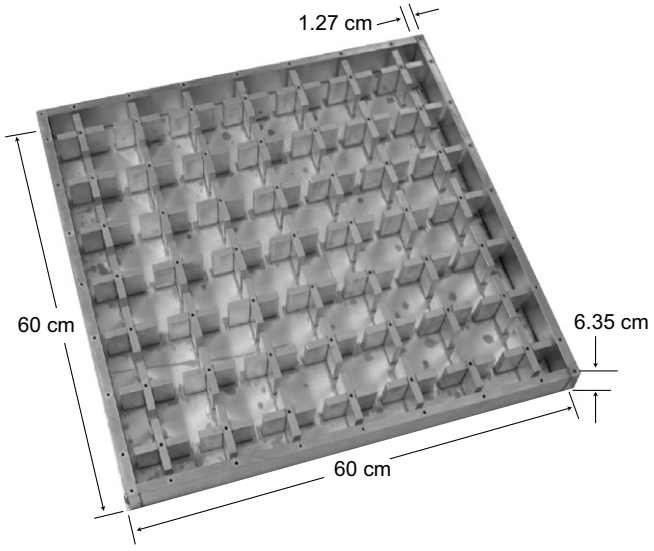

Fig. 6. Photograph of the as-brazed flat heat pipe sandwich panel.

contact with nickel, the equilibrium height of water in a cylindrical pore with a radius r can be predicted by Eq. (3) [43].

Eq. (3) can be used as a first order approximation for a stochastic open-cell nickel foam and its validity determined experimentally. Approximately 25 mm wide, ~300 mm long strips of foam were cut and compressed (in thickness) by varying amounts to decrease the effective pore diameter in the capillary pumping direction. To ensure good wetting, the nickel foams were thermally cleaned at 800 °C for 60 min, under a partial pressure (~250 mTorr) of a 96% argon, 4% hydrogen gas mixture. The strips were subsequently suspended in a container of deionized water, as shown in Fig. 2b, and the equilibrium height of the water rise measured.

Assuming that during compression, deformation is constrained in the through thickness direction, the effective pore diameter, d, of the compressed foam depends on the degree of compression and is approximated by

$$d = d_0 \frac{\delta}{\delta_0} \tag{4}$$

where d_0 is the initial average pore size of the as-received foam (~600 μm), δ the thickness of the compressed foam and δ_0 the thickness of the as-received foam (1.95 mm). Fig. 3a–e shows electron micrographs of the compressed nickel foam wicks for varying compression ratios ($\delta/\delta_0 = 1.0$, 0.75, 0.5, 0.25, 0.1). When stochastic open-cell foams are compressed in the through thickness direction, the pore morphology evolves from a series of interconnected circular pores to a series of interconnected pancake shaped pores. Fig. 4 shows the experimentally measured equilibrium height for the compressed nickel foams and the predicted capillary rise in a single tube of equivalent pore size. Also shown in Fig. 4 is the corresponding effective pore diameter, d, calculated from Eq. (4).

It can be seen that good agreement exists between the stochastic open-cell foam and a "equivalent" single cylin-

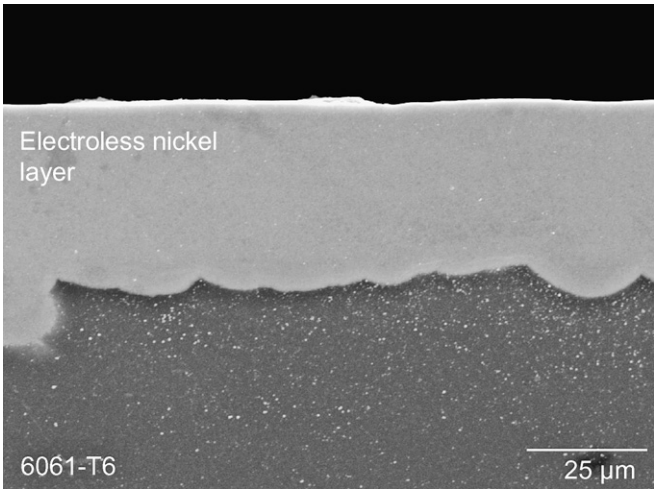

Fig. 7. Scanning electron micrograph of a cross section of the electroless nickel plating exhibiting a smooth, fully dense plating layer.

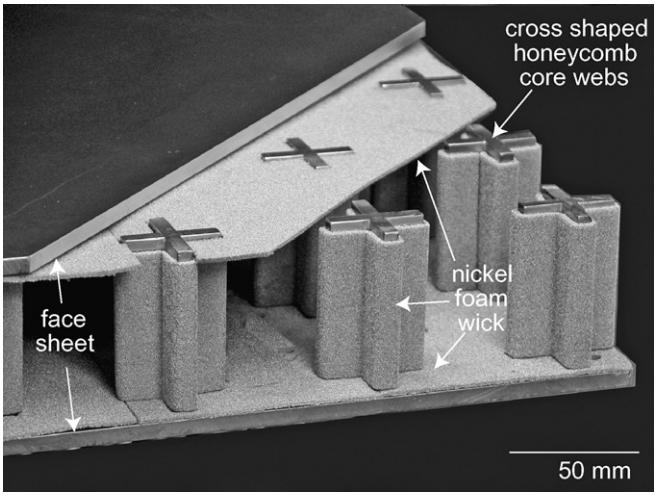

Fig. 8. Photograph of a representative cross section of the fully assembled flat heat pipe sandwich panel.

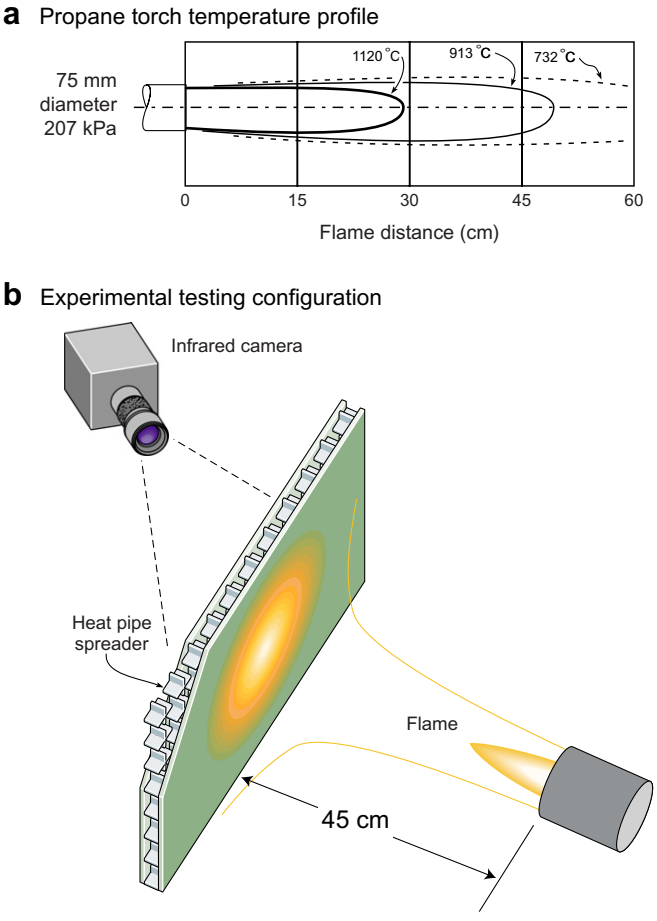

Fig. 9. Schematic illustration of (a) the approximate temperature profile of the propane torch at 207 kPa nominal operating pressure and (b) the testing orientation showing the heat source directed at the center of the front surface and the IR camera used for imaging the back surface temperature distribution.

drical pore predictions. The experimental values of the stochastic foam fall below the predicted values of a single cylindrical pore but follow the same trend and have been attributed to the tortuous pore morphology of the stochastic foam (which has not been accounted for in the model).

2.3. Thermodynamic modeling

From the first law of thermodynamics, the thermal energy (heat) stored by a flat heat pipe can be expressed as

$$Q = (m_{Al}C_{Al} + m_{Ni}C_{Ni})\Delta T + m_w(u_f - u_i) \quad (5)$$

where m_{Al}, m_{Ni} and C_{Al}, C_{Ni} are the mass and specific heat of 6061 aluminum and nickel, ΔT is the temperature difference ($T_f - T_i$) between the final and initial states, m_w is the mass of water in the system and ($u_f - u_i$) is the internal energy change of the working fluid. A more detailed description of the thermal capacity analysis for the flat heat pipe sandwich panel is provided in Appendix A.

Fig. 5a and b shows the predicted temperature and pressure in the flat heat pipe sandwich panel as a function of wick thickness. The curves shown in Fig. 5 serve as a performance map for the sandwich panel as a function of wick thickness. For the interior plate dimensions outlined in Section 2.1 and assuming the wick covers all internal surfaces uniformly, a wick thickness of 6.35 mm chokes off vapor flow between cruciform elements and a wick thickness of 8.8 mm completely fills the entire vapor space. The region

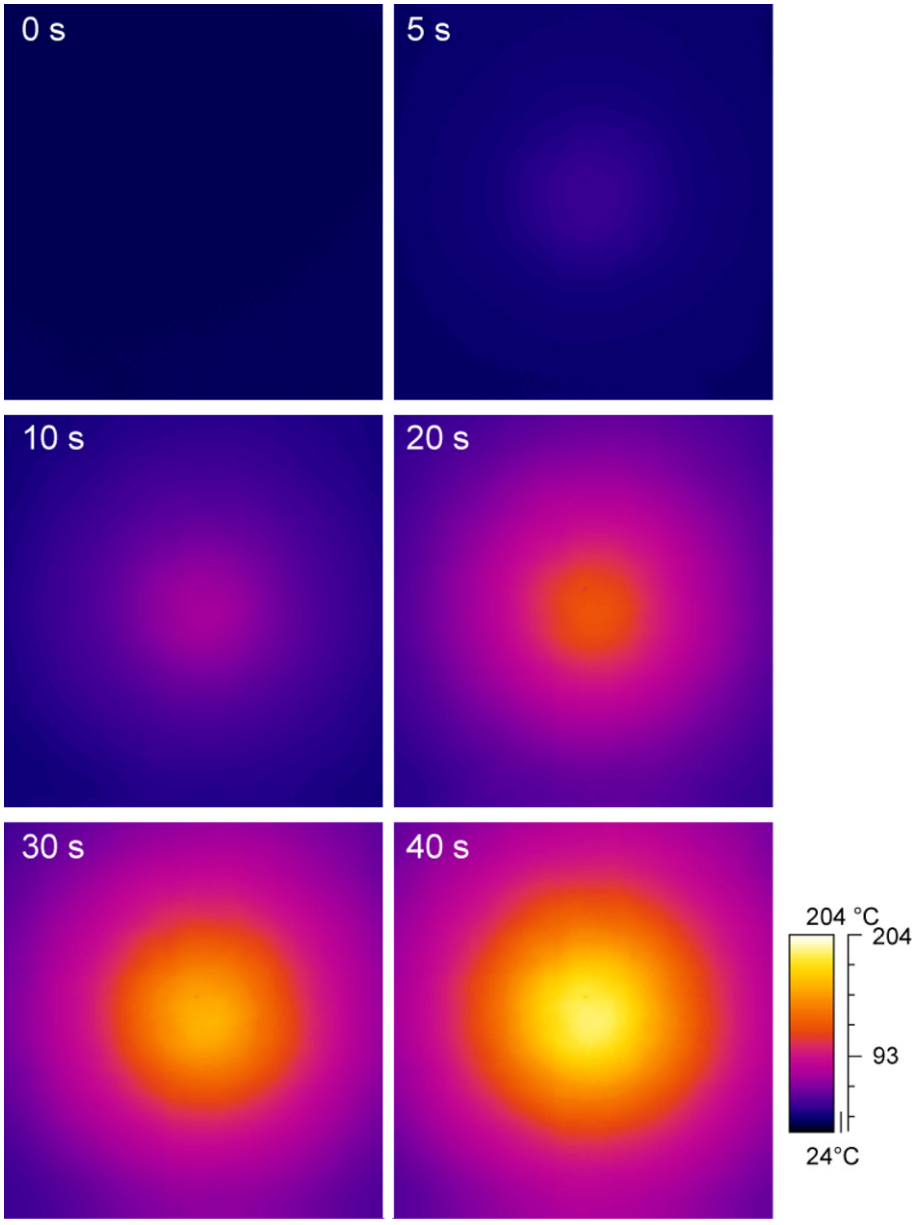

Fig. 10. The experimental measured temperature distribution on the back-side of a solid 6061-T6 aluminum plate during for heating of 0, 5, 10, 20, 30 and 40 s.

of practical interest is the saturated two-phase region, in which the liquid and vapor phases coexist at a uniform temperature and pressure throughout the system. Operation of the heat pipe sandwich panel in the superheated vapor domain is undesirable since any additional heat input drives the temperature rapidly upwards and operation in the subcooled liquid domain should also be avoided since the pressure increases rapidly and could result in catastrophic failure. The selection of a wick thickness of ~2 mm ensures operation in the saturated two-phase domain.

2.4. Sandwich panel fabrication

The design methodology previously described was evaluated by fabricating a 0.6 m × 0.6 m × 0.064 m thick square honeycomb sandwich panel using two 6.35 mm thick 6061 aluminum alloy face sheets and a 50.8 mm thick core. To ensure the wick could pump water at least half the panel length against a one-*g* gravitational force, a nickel foam wick compression of 1 mm was selected. After machining, all parts were dip cleaned in a 50–65 °C air agitated soap bath, tap water rinse, then dipped for 20–40 s in a 5–10% caustic soda solution at 70–80 °C, tap water rinsed and exposed to a 30 s treatment in a Gilsparkel acid solution. The samples were then tap water rinsed, dip treated in a deoxidizer (Allied Kellite #184) and again tap water rinsed. The rigorous pre-plating cleaning process (to remove surface contaminants and oxide layers) is a crucial step in the quality of electroless nickel plating. A 0.076 mm thick brazing foil (Lucas–Milhaupt, alloy 718; 88% Al, 12% Si) was placed between all surfaces to be brazed and the

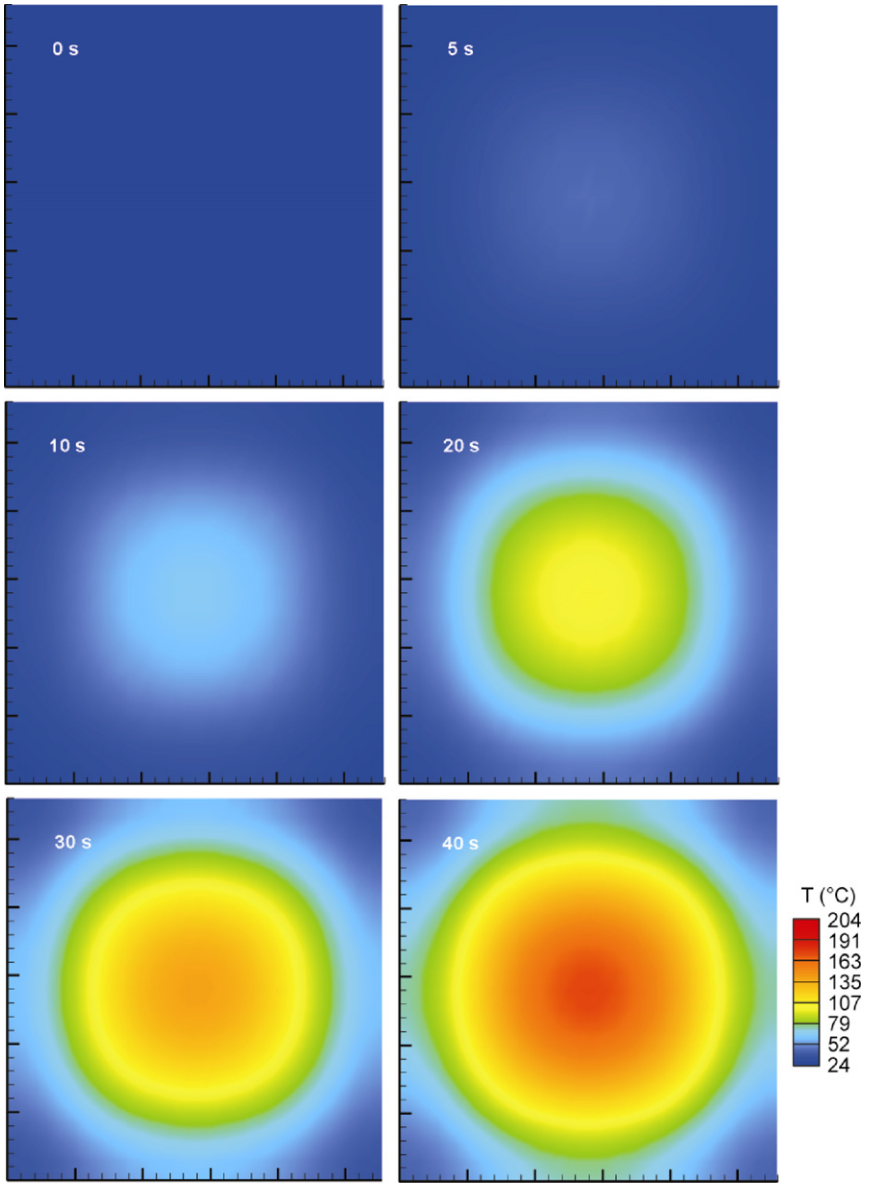

Fig. 11. The simulated temperature distribution on the back-side of a solid 6061-T6 aluminum plate during for heating of 0, 5, 10, 20, 30 and 40 s.

assembly adequately fixtured to prevent movement during the brazing operation. The assembly was placed in a pre-heat furnace at 538 °C ± 28 °C for 30 min, then transferred to a molten salt bath at 593 °C ± 6 °C for 5 min, followed by a rapid air quench. A post-brazing cleaning treatment similar to that used for pre-brazing was used to clean the structure prior to aging to a T4 (natural aged) condition. Fig. 6 shows a photograph of the as-brazed truncated-square honeycomb pipe sandwich panel.

After dip brazing, all internal surfaces that would be in contact with the working fluid were electroless nickel plated in accordance with SAE-AMS-C-26074 [44]. Electroless nickel deposition is an autocatalytic chemical reduction process where all conducting surfaces in contact with the plating solution are coated uniformly (regardless of the local geometry). This process was chosen because of the high quality and uniformity of the electroless process compared to electrolytic deposition where the coating uniformity depends upon the local current density [45]. Prior to electroless plating, the sample was degreased and alkaline cleaned to obtain maximum plating-substructure adhesion. After plating, the sample was heated to 120 °C (in air) for 1 h to increase adhesion of the nickel deposit. Fig. 7 shows a cross section micrograph of the electroless nickel plating indicating the good adherence and high density of the plating layer.

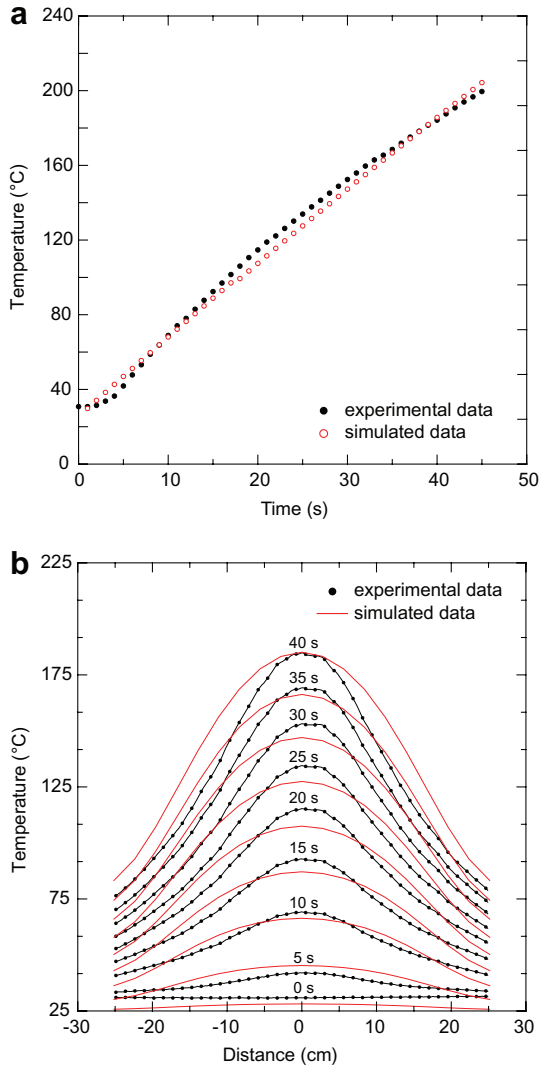

Fig. 12. (a) Shows the peak temperatures (coincident with the center heat source location) and (b) shows the centerline profile as a function of time during initial heating for the solid 6061-T6 aluminum plate.

The electroless nickel plated surfaces were cleaned with a mild acid solution of DURACLEAN 1075 (Duratech Industries, Inc., Orange, CA) and thoroughly rinsed with deionized water. DURACLEAN 1075 (dodecyclebenzene sulfonic acid 3% w/w) is an acid cleaning concentrate designed to clean oxide, tarnish and light oils from copper substrates and was used after determining the electroless nickel surfaces were readily wet with deionized water.

The compressed nickel foam wick sheet was water jet cut to size and formed to cover all internal surfaces. The wick components were thermally cleaned (at 800 °C for 60 min in a 96% argon, 4% hydrogen gas atmosphere at 250 mTorr) prior to insertion into the flat heat pipe structure. A 2 mm thick layer of wick was inserted against the face sheet, then 2 mm thick pre-formed wicks were slipped over the cruciform posts of the thermal spreader and another 2 mm thick layer placed against the opposite face sheet. Individual layers of wick were compressed to ~1.0 mm and sintered together at 1100 °C for 60 min forming the 2 mm thick wick structure. The back face of the flat heat pipe was fastened to the brazed structure via 2024-T4 aluminum machine screws. All edges and screw holes were sealed with a high-temperature silicone gasket sealant (Permatex 26B, Solon, OH). Fig. 8 shows a photograph of a representative cross section of an assembled flat heat pipe fabricated by methods similar to that described above.

The flat heat pipe sandwich panel was evacuated to a pressure of $\sim 10^{-4}$ Torr and charged with 1.625 l of deionized water and sealed with a needle valve. The working fluid volume was calculated to sufficiently fill the entire wick structure and provide a 20% overcharge to reduce the possibility of dry-out during experimental testing [19].

3. Results and analysis

Several experimental tests with the flat heat pipe sandwich panel were conducted to measure the transient response during heating and to compare this to an approximate equivalent areal density 6061-T6 solid aluminum plate. Heating was accomplished using a 75 mm diameter propane torch with a thermal power of 146.5 kW. Fig. 9a shows a schematic illustration of the approximate temperature profile of the propane torch at its 207 kPa nominal operating pressure. The samples were vertically oriented with the heat source directed at the center point and an infrared (IR) camera arranged to measure the back-side temperature distribution, Fig. 9b. The distance from the torch to the samples was ~45 cm. A ThermaCAM SC3000 IR camera with a spectral response of 8–9 μm

nominal, and a temperature accuracy of ±2 °C was used to monitor the samples thermal field. The back-side of both samples was painted with a high-temperature paint to provide a uniform emissivity near unity.

3.1. Solid aluminum plate

Solid plate experiments were first conducted to deduce the non-uniform heat flux distribution of the propane torch. A 12.7 mm thick 6061-T6 aluminum plate was heated for ~40 s, while monitoring the back-side surface temperature at 1 s intervals using the arrangement shown in Fig. 9b. Fig. 10 shows the experimentally measured temperature distribution on the back-side for heating times of 0, 5, 10, 20, 30 and 40 s. The development of a hot spot at the center of the plate can be clearly seen.

The back surface thermal flux distribution can be estimated using an energy balance for the solid aluminum plate assuming transport by conduction and natural convection cooling at the back-side (the radiative component was assumed small at this test temperature). The components estimated heat transfer coefficient was ~5 W/m^2 K. An iterative numerical analysis of the resulting heat flux distribution was then used to infer the incident heat flux with details given in Carbajal et al. [32]. The numerical modeling indicates that the heat flux generated on the solid flat plate can be approximated by a probabilistic function with a maximum heat input at the impingement point of ~42 kW and a minimum at the edges of the plate of ~8.5 kW [32]. The numerically calculated temperature distributions on the back side are shown in Fig. 11 and are in good agreement with the experimental images of Fig. 10 [46]. Fig. 12a shows the experimental and simulated peak temperatures (at the center of the heat source impingement point) on the back side of the solid plate as a function of time. Fig. 12b shows the predicted temperature variation

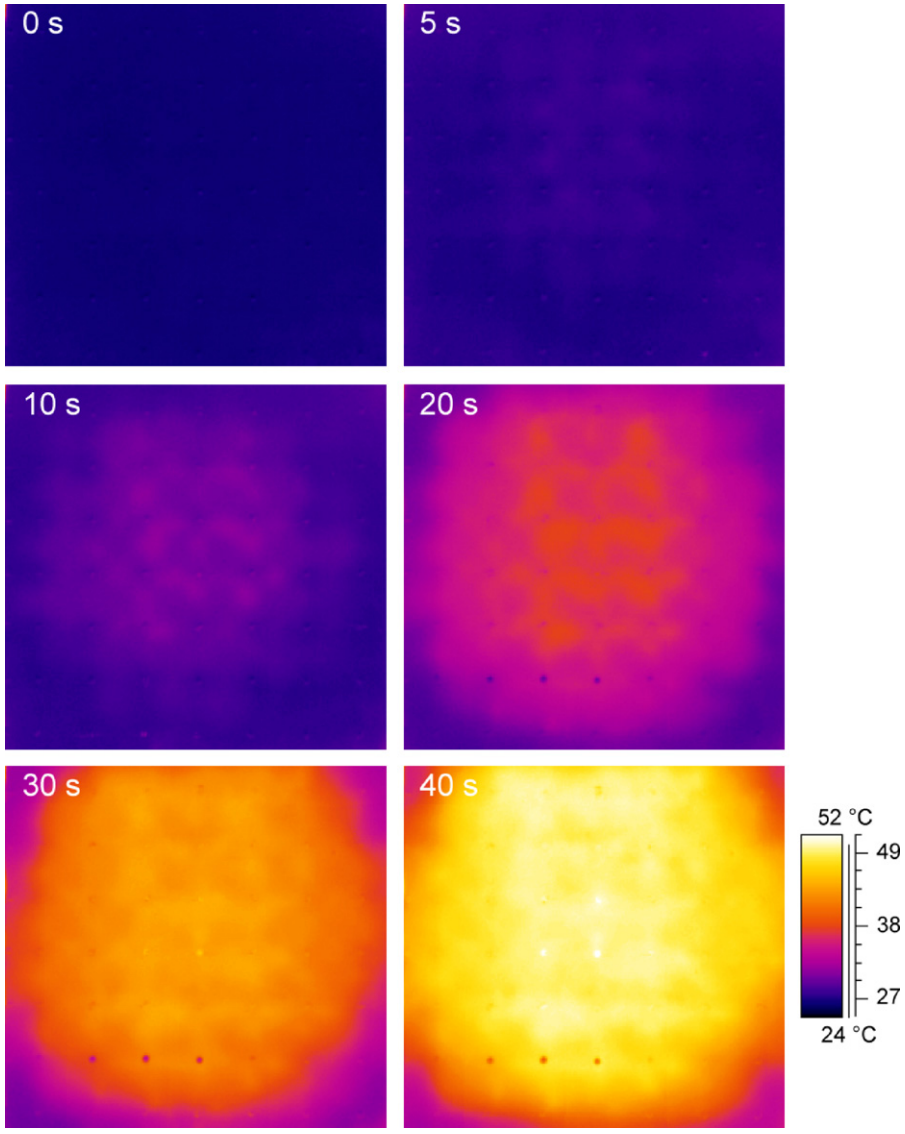

Fig. 13. The experimental measured temperature distribution on the back-side of the flat heat pipe sandwich panel during for heating of 0, 5, 10, 20, 30 and 40 s.

across the centerline on the back side of the solid 6061-T6 aluminum plate for heating times of 0, 5, 10, 15, 20, 25, 30, 35 and 40 s. This numerically generated function was used as the heat flux input for the modeling of the flat heat pipe sandwich panel described in the next section.

3.2. Flat heat pipe response

The flat heat pipe sandwich panel was heated for 40 s, while monitoring the back-side surface temperature at 1 s intervals using the arrangement shown in Fig. 9b. Fig. 13 shows the measured back-side temperature distribution for heating times of 0, 5, 10, 20, 30 and 40 s. It can be clearly seen that the hot spot is much more dispersed about the center of the plate compared to that of the solid plate experiments, Fig. 10. In addition, the maximum temperature on the back side of the flat heat pipe sandwich panel was significantly reduced compared to the solid plate. This is consistent with the significantly higher thermal capacity of the flat heat pipe sandwich panel.

The numerical expression developed for the heat flux at the front side of the solid plate was applied to a finite difference model of the flat heat pipe sandwich panel (see Ref. [32] for the details of this model). It was assumed that the flat heat pipe sandwich panel was subjected to the same heat flux boundary conditions as the front face of the solid plate. A heat transfer analysis was performed for the flat heat pipe sandwich panel which incorporated conduction, convection and phase change [32]. Natural convection with an estimated heat transfer coefficient of $\sim 5\ W/m^2\ K$ and radiation were considered at the back side of the plate. The numerically simulated temperatures shown in Fig. 14 were found to be in good agreement with the experimental data. Fig. 15a shows the experimental and simulated peak

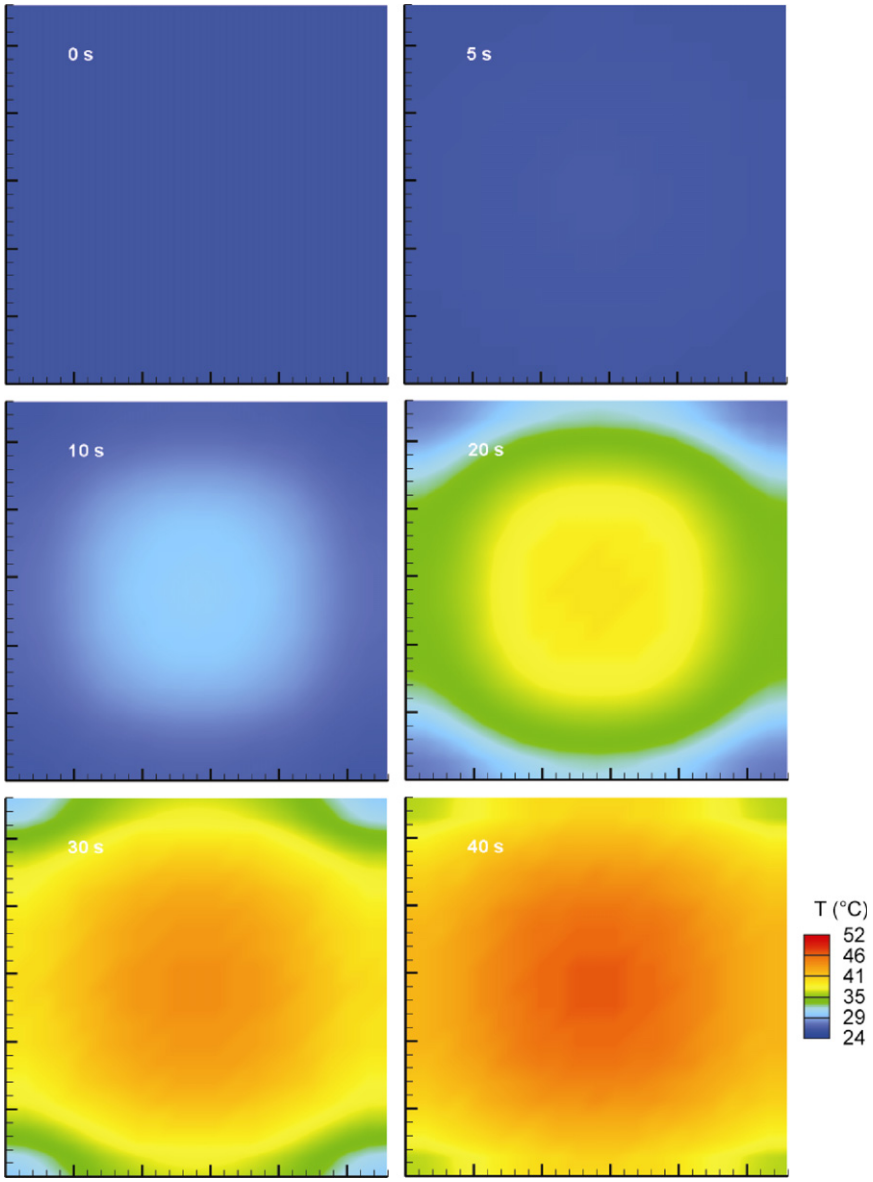

Fig. 14. The model predicted temperature distribution on the back-side of the flat heat pipe sandwich panel for heating times of 0, 5, 10, 20, 30 and 40 s.

temperatures (directly opposite the center of the heat source) as a function of time. Again, the numerically simulated peak temperatures are found to be in good agreement with the experimental data.

Fig. 15b shows the temperature variation across the centerline on the back side of the flat heat pipe. During early stages of transient heating (up to ~25 s) slight irregularities in the experimental data coincided with the location of the crucifix shaped supports. They act as initial high thermal conductivity pathways and a component of the applied heat flux rapidly propagates from the front to back face causing small peaks in the temperature profile data of Fig. 15b and the grainy texture in the IR images of Fig. 13. These local temperature fluctuations are not present in the simulated results, Fig. 14, because a lump parameter estimate methodology which homogenizes the core properties was used in the finite difference model [32]. The overall system remained at relatively low temperatures compared with the solid plate due to its high inherent thermal capacity. After heating for more than 25 s, the temperature distribution became more uniform across the centerline due to the increased vapor transport contribution of the heat pipe. This resulted in significant flattening (spreading) of the temperature profile. The reader is referred to Carbajal et al. [32] for additional description of the numerical simulations as well as detailed analysis of the temperature distribution at the evaporator and condenser plates, the temperature fields within the flat heat pipe system and the velocity distributions in the wick and vapor core regions during initial transient heating.

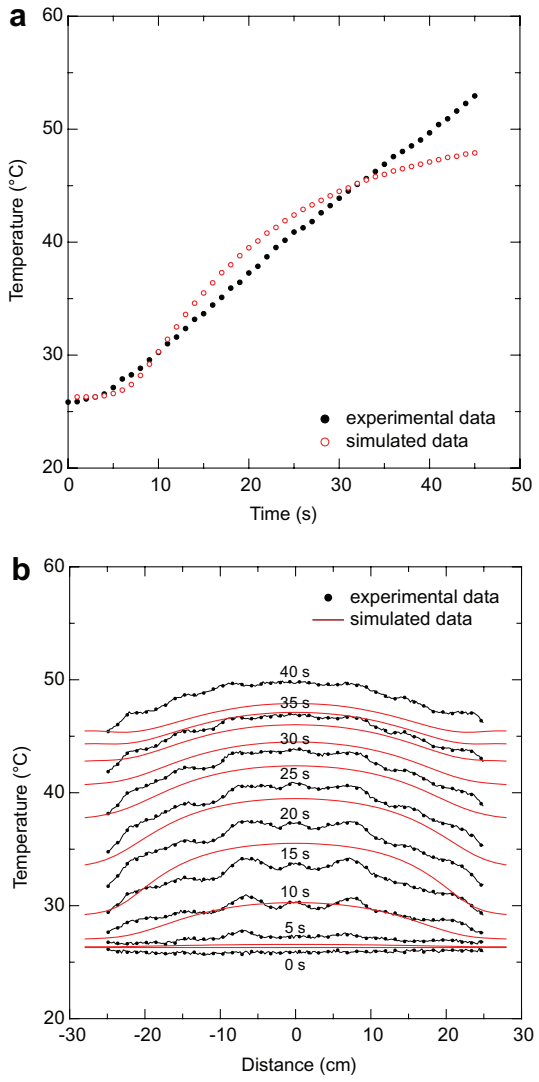

Fig. 15. (a) The maximum temperature (opposite the center of the heat source). (b) The centerline temperature profile as a function of time during initial heating for the flat heat pipe sandwich panel.

4. Discussion

A multifunctional structural load supporting heat pipe sandwich panel has been designed and constructed using a high-strength, nickel plated aluminum alloy. Modified open-cell nickel foam has been used for the wick structure and water as the working fluid. Thermodynamic design principles for a multifunctional heat pipe sandwich panel have been developed and used to guide the fabrication and an experimental assessment its performance for an applied localized heat flux has been conducted. The heat flux distribution from a propane torch was first determined by modeling the temperature field of a solid panel and using the free parameters of an assumed heat flux profile to best fit predictions to measurements. This heat flux distribution was used as the input to a finite difference model of the conductive, convective and radiative heat transfer processes within the core of the flat heat pipe sandwich panel. The temperature distribution predictions on the condenser side of the flat heat pipe sandwich panel agree well with the experimental measurements. The maximum temperature of the heat pipe panel is significantly lower than an equivalent areal density solid plate indicative of its high thermal capacitance.

The heat capacity of the flat heat pipe sandwich panel can be estimated for prescribed initial and final temperatures assuming thermal equilibrium is achieved between all of the components (i.e. the aluminum structural sandwich panel, the stochastic open-cell nickel foam and the working fluid). In that case, the heat stored depends only on the initial and final states and is independent of the path taken. If no heat rejection occurs (i.e. the heat input into the flat heat pipe is equivalent to the heat stored by the system), such an analysis can be used to estimate the maximum thermal capacity for the flat heat pipe sandwich panel.

Fig. 16a shows the computed heat capacity of the heat pipe sandwich panel (for $\Delta T = 50$, 75 and 100 °C) estimated from Eq. (5) assuming thermal equilibrium exists between all the components of the system. It is seen that as the water saturated wick thickness, δ, and temperature difference, ΔT, increase; the overall heat capacity (Q) of the system also increases. However, as the wick thickness and amount of water in the system increases, the corre-

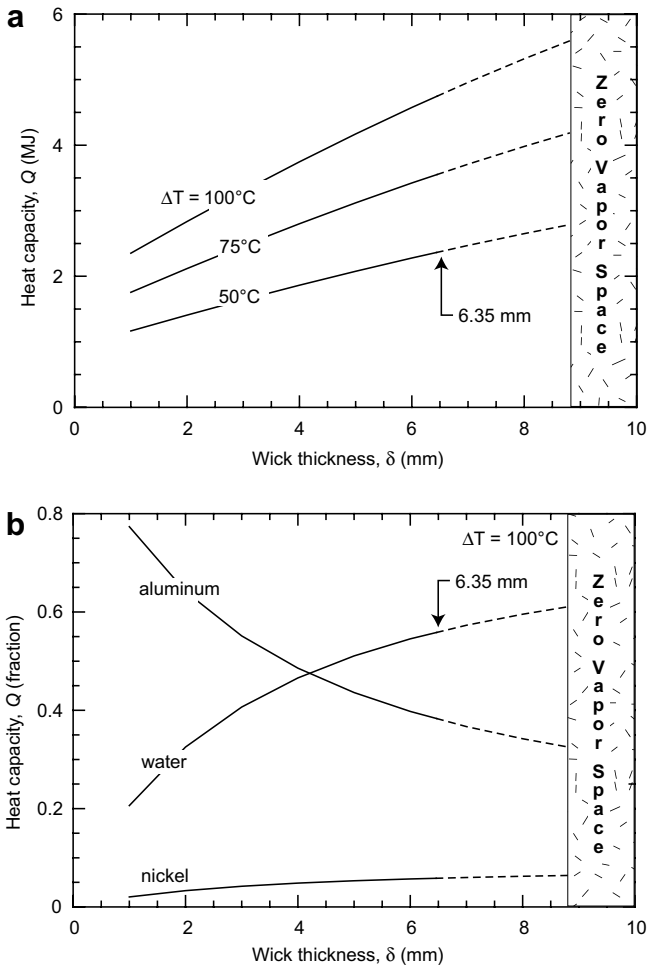

Fig. 16. (a) The heat capacity of the flat heat pipe sandwich panel. (b) The relative fraction of the heat capacity due to the aluminum, nickel and water components of the flat heat pipe sandwich panel. The data shown in (b) is for $\Delta T = 100$ °C.

sponding vapor volume decreases. Therefore, the fraction of the heat stored in the various components of the panel varies with δ. Fig. 16b shows the normalized fraction of the overall heat capacity for the aluminum, nickel and water components of the flat heat pipe sandwich panel. There was a negligible affect of ΔT on the fraction of the heat capacity between the components and the data shown in Fig. 16b is for $\Delta T = 100$ °C.

5. Summary

- A multifunctional flat heat pipe sandwich panel with a honeycomb core combining load support and thermal management has been designed using thermodynamic and heat transport models.
- The approach utilizes a nickel plated, high-strength aluminum alloy for structural load support, an open-cell nickel foam for wicking and deionized water as the working fluid.
- The design principles have been verified by fabricating and experimentally validating the operational principles and thermal spreading characteristics of a heat pipe sandwich panel.
- The thermal response of the model system has been measured and the experimental data and associated finite difference model data are found to be in good agreement.

Acknowledgements

The authors would like to acknowledge joint support from the Defense Advanced Research Projects Agency (Leo Christodoulou, program manager) and the Office of Naval Research under Grant Number N00014-04-1-0299. In addition, the authors would like to thank Don Jordan and Jessica Sheehan of the University of Virginia for their help with the experimental testing facility. DARPA Distribution Statement A: approved for public release, distribution unlimited.

Appendix A. Thermodynamic analysis

To fully understand the thermodynamic state of the flat heat pipe sandwich panel, it is necessary to know the mass of the working fluid in the liquid and vapor phases at the initial and final states using a thermodynamic analysis. As a first order approximation, the wick was assumed to be fully saturated with water and the structure was assumed to be at thermodynamic equilibrium.

The volume of the liquid, V_l, and vapor, V_v, phases are dependant on the geometry of the system, the thickness and porosity of the nickel wick. All pertinent dimensions of the flat heat pipe sandwich panel are described in Section 2.4.

The total mass of water, m_i, in the heat pipe sandwich panel (at an initial temperature T_i) is

$$m_i = m_{li} + m_{vi} \tag{A.1}$$

where, m_{li} and m_{vi} are the masses of the liquid and vapor phases respectively and are represented by

$$m_{li} = \frac{V_l}{v_l} \quad \text{and} \quad m_{vi} = \frac{V_v}{v_v} \tag{A.2}$$

where V_l and V_v are the volumes of liquid and vapor and v_l and v_v are the specific volumes of the saturated liquid and vapor phases.

Assuming saturation condition at the initial state, Table A1 shows the physical properties of water at $T_0 = 26.3$ °C.

Table A1
Physical properties of water at 26.3 °C

Saturation pressure	6561.49 Pa
Specific volume (saturated liquid)	$V_l = 0.001003$ m^3/kg
Specific volume (saturated vapor)	$V_v = 40.31$ m^3/kg
Specific internal energy (saturated liquid)	110.69^3 J/kg
Specific internal energy (saturated volume)	2410.62×10^3 J/kg

The quality, x_i (defined as the mass of the vapor phase divided by the total mass of the liquid and vapor phases), of the initial state is

$$x_i = \frac{m_{vi}}{m_i} \tag{A.3}$$

From Eq. (A.3) it can be shown that the initial quality depends on the wick thickness and the initial temperature. Once the initial quality has been computed it defines the other thermophysical properties of the working fluid at the initial state, such as the specific internal energy (u):

$$u_i = u_{li} + x_i \cdot (u_{vi} - u_{li}). \tag{A.4}$$

By applying a thermodynamic analysis for any amount of heat input applied to the system, it is possible to determine the temperature, T_f, at the final state. Applying an energy balance to the closed, rigid system in thermal equilibrium and assuming a no heat is rejected and no sensible heating of the aluminum case occurs, we can write:

$$Q_{=} m_f u_f - m_i u_i + \rho_{Al} V_{Al} C_{Al} (T_f - T_i) + \rho_{Ni} V_{Ni} C_{Ni} (T_f - T_i) \tag{A.5}$$

where V_{Al}, and V_{Ni} are the volumes, ρ_{Al}, and ρ_{Ni} are the densities and C_{Al}, and C_{Ni} are the specific heats of the aluminum case and nickel wick material. Table A2 shows the physical properties of 6061-T6 aluminum and nickel at $T_0 = 26.3$ °C.

Eq. (A.8) can be solved for the specific internal energy in the final state and is

$$u_f = u_i + \frac{Q - [\rho_{Al} V_{Al} C_{Al} (T_f - T_i) + \rho_{Ni} V_{Ni} C_{Ni} (T_f - T_i)]}{m_i} \tag{A.6}$$

which represents an implicit formulation for the internal energy, u_f, and the final temperature, T_f. Note that $m_f = m_i$ because the system is closed.

Since the thermal process in a heat pipe is isochoric (constant volume), $v_f = v_i$. For pure substances such as water with only one quasi-static work mode, the thermodynamic state is defined by two independent variables, i.e., the specific internal energy (u) and specific volume (v). From these two independent variables it is possible to determine all of the other thermophysical properties at the final state. These variables can be readily computed from thermodynamic tables. This implies that the amount of vapor and liquid phase for a fixed total input heat (Q) can be determined as follows:

Table A2
Physical properties of 6061-T6 aluminum and nickel at 26.3 °C

Density (aluminum)	$\rho_{Al} = 2700$ kg/m^3
Density (nickel)	$\rho_{Ni} = 8900$ kg/m^3
Specific heat (aluminum)	0.9 kJ/kg K
Specific heat (nickel)	0.5 kJ/kg K

$$m_{vf} = x_f \cdot m_f \tag{A.7}$$

$$m_{lf} = m_f - m_{vf} \tag{A.8}$$

and the amount of evaporated water is

$$\Delta m = m_{lf} - m_{li} \tag{A.9}$$

which yields an evaporated volume of

$$\Delta V = \Delta m \cdot v_{lf} \tag{A.10}$$

Therefore, the temperature and pressure increases can be determined from the expressions:

$$\Delta T = T_f - T_i \tag{A.11}$$

$$\Delta P = P_f - P_i \tag{A.12}$$

References

[1] V.S. Deshpande, M.F. Ashby, N.A. Fleck, Foam topology bending versus stretching dominated architectures, Acta Mater. 49 (6) (2001) 1035–1040.

[2] H.N.G. Wadley, Multifunctional periodic cellular metals, Philos. Trans. Roy. Soc. A: Math. Phys. Eng. Sci. 364 (1838) (2006) 31–68.

[3] H.N.G. Wadley, Cellular metals manufacturing, Adv. Eng. Mater. 4 (10) (2002) 726–733.

[4] H.N.G. Wadley, Fabrication and structural performance of periodic cellular metal sandwich structures, Compos. Sci. Technol. 63 (16) (2003) 2331–2343.

[5] K.P. Dharmasena, H.N.G. Wadley, Z. Xue, J.W. Hutchinson, Mechanical response of metallic honeycomb sandwich panel structures to high intensity dynamic loading, Int. J. Impact Eng., in press.

[6] H.N.G. Wadley, K.P. Dharmasena, Y. Chen, P. Dudt, D. Knight, R. Charette, K. Kiddy, Compressive response of multilayer pyramidal lattices during underwater shock loading, Int. J. Impact Eng., in press.

[7] J. Tian, T. Kim, T.J. Lu, H.P. Hodson, D.T. Queheillalt, D.J. Sypeck, H.N.G. Wadley, The effects of topology upon fluid-flow and heat transfer within cellular copper structures, Int. J. Heat Mass Transfer 47 (14–16) (2004) 3171–3186.

[8] J. Tian, T.J. Lu, H.P. Hodson, D.T. Queheillalt, H.N.G. Wadley, Cross flow heat exchange of textile cellular metal core sandwich panels, Int. J. Heat Mass Transfer 50 (13–14) (2007) 2521–2536.

[9] T.J. Lu, J.W. Hutchinson, A.G. Evans, Optimal design of a flexural actuator, J. Mech. Phys. Solids 49 (9) (2001) 2071–2093.

[10] S.L. dos Santos e Lucato, J. Wang, P. Maxwell, R.M. McMeeking, A.G. Evans, Design and demonstration of a high authority shape morphing structure, Int. J. Solids Struct. 41 (13) (2004) 3521–3543.

[11] D.M. Elzey, A.Y.N. Sofla, H.N.G. Wadley, A shape memory-based multifunctional structural actuator panel, Int. J. Solids Struct. 42 (7) (2005) 1943–1955.

[12] T. Kim, C.Y. Zhao, T.J. Lu, H.P. Hodson, Convective heat dissipation with lattice-frame materials, Mech. Mater. 36 (8) (2004) 767–780.

[13] T. Kim, H.P. Hodson, T.J. Lu, Fluid-flow and endwall heat-transfer characteristics of an ultralight lattice-frame material, Int. J. Heat Mass Transfer 47 (6–7) (2004) 1129–1140.

[14] T. Kim, H.P. Hodson, T.J. Lu, Contributions of vortex structures and flow separation to local and overall pressure and heat transfer characteristics in an ultralightweight lattice material, Int. J. Heat Mass Transfer 48 (19–20) (2005) 4243–4264.

[15] S.A. Berggren, D. Lukkassen, A. Meidell, L. Simula, On stiffness properties of square honeycombs and other unidirectional composites, Compos. Part B: Eng. 32 (6) (2001) 503–511.

[16] F. Cote, V.S. Deshpande, N.A. Fleck, A.G. Evans, The out-of-plane compressive behavior of metallic honeycombs, Mater. Sci. Eng. A 380 (1–2) (2004) 272–280.

[17] F.W. Zok, H. Rathbun, H.E. Ferri, C. Mercer, R.M. McMeeking, A.G. Evans, Structural performance of metallic sandwich panels with square honeycomb cores, Philos. Mag. 85 (26–27) (2005) 3207–3234.
[18] S. Liang, H.L. Chen, Investigation on the square cell honeycomb structures under axial loading, Compos. Struct. 72 (4) (2005) 446–454.
[19] G.P. Peterson, An Introduction to Heat Pipes: Modeling, Testing and Applications, Wiley-Interscience, New York, NY, 1994.
[20] H.J. Tanzer, High-capacity honeycomb panel heat pipes for space radiators, in: AIAA-1983-1430, Proceedings of 18th AIAA Thermophysics Conference, Montreal, Canada, 1983.
[21] H.J. Tanzer, G.L. Fleischman, J.G. Rankin, Honeycomb panel heat pipe development for space radiators, in: AIAA-1985-978, Proceedings of 20th Thermophysics Conference, Williamburg, VA, 1985.
[22] H.J. Tanzer, High capacity demonstration of honeycomb panel heat pipes, NASA CR-181776, 1989.
[23] M. Cerza, B. Boughey, K.W. Lindler, A flat heat pipe for use as a cold side heat sink, in: Intersociety Energy Conversion Engineering Conference and Exhibit (IECEC), 35th, Las Vegas, NV, Collection of Technical Papers, vol. 2 (A00-37701), 2000.
[24] M. Cerza, B. Boughey, K.W. Lindler, Flat heat pipe design, construction and analysis, in: Intersociety Energy Conversion Engineering Conference and Exhibit (IECEC), 34th, Vancouver, BC, 1999-01-2527, 1999.
[25] A. Basiulis, C.J. Camarda, Design, fabrication and test of liquid metal heat-pipe sandwich panels, in: AIAA-1982-903, Proceedings of 3rd Joint Thermophysics, Fluids, Plasma and Heat Transfer Conference, St. Louis, MO, 1982.
[26] C.J. Camarda, A. Basiulis, Radiant heating tests of several liquid–metal heat-pipe sandwich panels, J. Spacecraft Rockets 21 (1) (1984) 4–5.
[27] D.R. Tenney, W.B. Lisagor, S.D. Dixon, Materials and structures for hypersonic vehicles, J. Aircraft 26 (11) (1989) 953–970.
[28] G.F. Pittinato, Hydrogen gas generation in water heat pipes, J. Eng. Mater. Technol. 100 (3) (1978) 313–318.
[29] P.D. Dunn, D.A. Reay, Heat Pipes, fourth ed., Pergamon, Oxford, 1994.
[30] W.T. Anderson, Hydrogen evolution in nickel-water heat pipes, in: AIAA-1973-726, Proceedings of 8th Thermophysics Conference, Palm Springs, CA, 1973, pp. 1–7.
[31] A. Basiulis, R.C. Prager, Compatibility and reliability of heat-pipe materials, in: AIAA-75-660, Proceedings of 10th Thermophysics Conference, Denver, CO, 1975, pp. 515–529.
[32] G. Carbajal, C.B. Sobhan, G.P. Peterson, D.T. Queheillalt, H.N.G. Wadley, Thermal response of a flat heat pipe sandwich structure to a localized heat flux, Int. J. Heat Mass Transfer 49 (21–22) (2006) 4070–4081.
[33] M.J. Silva, L.J. Gibson, The effects of non-periodic microstructure and defects on the compressive strength of the two-dimensional cellular solids, Int. J. Mech. Sci. 39 (5) (1997) 549–563.
[34] C. Chen, T.J. Lu, N.A. Fleck, Effects of imperfections on the yielding of two-dimensional foams, J. Mech. Phys. Solids 47 (11) (1999) 2235–2272.
[35] X.E. Guo, L.J. Gibson, Behavior of intact and damaged honeycomb: a finite element study, Int. J. Mech. Sci. 41 (1) (1999) 85–105.
[36] A.J. Wang, D.L. McDowell, Effects of defects on in-plane properties of periodic metal honeycombs, Int. J. Mech. Sci. 45 (11) (2003) 1799–1813.
[37] A.J. Wang, D.L. McDowell, In-plane stiffness and yield strength of periodic metal honeycombs at intermediate relative density, J. Eng. Mater. Technol. 126 (2) (2004) 137–156.
[38] F.W. Zok, personal communication.
[39] S.W. Chi, Heat Pipe Theory and Practice, McGraw-Hill, New York, NY, 1976.
[40] V. Paserin, S. Marcuson, J. Shu, D.S. Wilkinson, CVD technique for Inco nickel foam production, Adv. Eng. Mater. 6 (6) (2004) 454–459.
[41] F.A.L. Dullien, Porous Media: Fluid Transport and Pore Structure, Academic Press, Burlington, MA, 1992.
[42] E.W. Washburn, The dynamics of capillary flow, Phys. Rev. 17 (3) (1921) 273–283.
[43] D.R. Lide, Handbook of Chemistry and Physics, 71st ed., CRC Press, Boca Raton, FL, 1990.
[44] SAE-AMS-C-26074, Coatings, Electroless Nickel, Requirements for, SAE International, Warrendale, PA. <www.sae.org>.
[45] M. Schlesinger, Electroless deposition of nickel, in: M. Schlesinger, M. Paunovic (Eds.), Modern Electroplating, fourth ed., John Wiley & Sons Inc., Hoboken, NJ, 2000, pp. 667–684.
[46] G. Carbajal, C.B. Sobhan, G.P. Peterson, D.T. Queheillalt, H.N.G. Wadley, A quasi-3D analysis of the thermal performance of a flat heat pipe, Int. J. Heat Mass Transfer, in press, doi:10.1016/j.ijheatmasstransfer.2007.01.057.